Available online at www.sciencedirect.com

ScienceDirect

Journal of Sound and Vibration 310 (2008) 1014–1035

JOURNAL OF
SOUND AND
VIBRATION

www.elsevier.com/locate/jsvi

Scattering of acoustic duct modes by axial liner splices ☆

Christopher K.W. Tam[a,*], Hongbin Ju[a], Eugene W. Chien[b]

[a]*Department of Mathematics, Florida State University, Tallahassee, FL 32306-4510, USA*
[b]*Goodrich Aerostructures Group, Chula Vista, CA 91912-0878, USA*

Received 25 May 2006; received in revised form 16 August 2007; accepted 20 August 2007
Available online 17 October 2007

Abstract

Recent engine test data and results of computational analysis show that the engine inlet acoustic liner splices have a significant impact on aircraft flight noise certification and cabin noise levels. The phenomenon of scattering of acoustic duct modes by axial liner splices is investigated. Previous studies, invariably, follow the frequency-domain approach. The present study, however, uses the time-domain approach. It is demonstrated that time-domain computation yields results that are in close agreement with frequency-domain results. The scattering phenomenon under consideration is very complex. This study concentrates on the effects of four parameters. They are the width of the splices, the frequency of the incident duct mode, the number of splices and the length of splices. Based on the computed results, the conditions under which scattered wave modes would significantly increase the intensity of transmitted waves are identified. It is also found that surface scattering by liner splices has the tendency to distribute energy equally to all the cut-on scattered azimuthal modes. On the other hand, for each scattered azimuthal mode, the high-order cut-on radial mode, generally, has the highest intensity. Moreover, scattering by liner splices is a local phenomenon. It is confined primarily to an area of the duct adjacent to the junction between the hard wall near the fan face and the spliced liner.

1. Introduction

Scattering takes place when an acoustic duct mode propagates into a region of a circular duct lined with sound absorbing material and hard wall splices. An incident duct mode is often scattered into a multitude of other azimuthal and radial modes depending on the number and width of the splices. If the frequency of the incident duct mode is slightly higher than the cut-on frequency, the energy flux of the scattered acoustic modes may be many decibels higher than that of the incident acoustic mode at the exit end of the spliced liner. This is a most undesirable situation.

Recently, the phenomenon of duct mode scattering by axial liner splices has attracted a good deal of interest. In an early work, Fuller [1,2] used duct mode expansions to investigate the scattering effect. More recently, Regan and Eaton [3] studied the problem using finite element formulation in the frequency domain. The finite element method leads immediately to a large matrix system as in the case of Fuller. To obtain an

---

☆ A portion of this paper was presented at the 12th AIAA/CEAS Aeroacoustics Conference, Cambridge, MA, 8–10 May 2006.

*Corresponding author.

E-mail address: tam@math.fsu.edu (C.K.W. Tam).

0022-460X/$ - see front matter © 2007 Elsevier Ltd. All rights reserved.
doi:10.1016/j.jsv.2007.08.027

accurate solution of a very large matrix system, as it turns out, is non-trivial. Elnady et al. [4] devised a point matching method to model the spliced liner surface. This method again results in the need to solve a large matrix system. In a follow-up work, Elnady and Boden [5] used the point matching method to study the effect of hard wall splices for both locally reacting and non-locally reacting liners. They concluded that non-locally reacting liners were less affected by the presence of hard strips than locally reacting liners.

Bi et al. [6] studied sound propagation in ducts with varying cross-section and with non-uniform impedance. They expanded their solutions using the propagating duct modes as basis functions. As in most eigenfunction expansion methods, the proper choice of a set of basis functions is crucial. However, there is no obvious and simple choice. Bi et al. considered the use of rigid wall duct modes. But they are not the natural modes of a lined duct. The use of locally parallel duct modes with liners might seem to be a better choice. Unfortunately, for eigenmodes of a lined duct, there is no guarantee that the computed modes form a complete set of basis functions. In addition, the computation of these modes is by no means straightforward. Moreover, this expansion method will once more lead to a large matrix that may be dense and not easy to solve. In a related work by Bi et al. [7], this duct mode expansion method was used to analyze the scattering of duct modes by rigid splices in lined ducts. Preliminary results for an incident mode at slightly above the cut-on frequency were reported. The influence of liner length, the azimuthal mode order of the incident duct mode, as well as axial non-uniformities were briefly considered.

McAlpine et al. [8] investigated the effect of spliced intake liner at supersonic fan tip speed. They employed a numerical code named ACTRAN for their computation. The ACTRAN code is based on the finite element method. For incident duct modes at typical blade passage frequency (BPF), their three-dimensional (3-D) finite element simulation required considerable amount of computing resources. To reduce computing requirements to a manageable level, they studied the problem at half-BPF of a typical commercial turbofan engine. The number of splices was also reduced to half while the liner length increased to twice the typical lengths. McAlpine et al. also used the Airbus-France boundary element code named ACTI3S in their study. They reported that the finite element ACTRAN code and the boundary element ACTI3S code yielded similar results for certain cases in their investigation. A major conclusion of their study is that fan speed is a critical factor of the splice scattering phenomenon and that thinner splices would reduce the level of scattered tones.

Recently, Tester et al. [9] performed a validation test of the Cargill analytical method for duct mode scattering by liner splices. The Cargill method is based on the Kirchhoff approximation. Its main advantage is simplicity. The validation test was carried out by comparing the results obtained by the Cargill method with those of the ACTRAN finite element code. Tester et al. reported that the ACTRAN and Cargill results agreed well for the no-flow case except for some minor discrepancies in the back-scattered modes. The back-scattered modes are of secondary importance compared to the forward scattered modes. When a mean flow up to Mach 0.4 was included, the agreement between the ACTRAN and Cargill results was still acceptable except again for the field dominated by back-scattering. In addition to validating the analytical method, Tester et al. unlike previous works, presented results for the axial variation in sound power level in each scattered azimuthal mode as well as the incident mode. This allows one to see where the scattered power is generated. Further, they showed that the scattered sound power level was almost independent of the azimuthal mode number.

In this work, a specially designed time-domain code based on the 7-point stencil time marching dispersion-relation-preserving (DRP) scheme is used to compute the scattered and transmitted acoustic duct modes. Previous works on this subject invariably use the frequency-domain approach. This study intends to demonstrate that the accuracy of the time-domain solution is, at least, comparable to that obtained by frequency-domain codes. One advantage of time-domain approach over frequency-domain method is that multiple frequencies and broadband input can be calculated in a single computation. Further, nonlinear effects may also be included. In this paper, however, the primary objective is to study the axial splice scattering phenomenon. These other computational issues will not be considered and will be left to a future work. In addition to the DRP scheme, advanced computational aeroacoustics (CAA) boundary conditions are used in the computation. They include time-domain impedance boundary conditions, ghost-point method (for enforcing boundary conditions) as well as the perfectly matched layer (PML).

The results of a parametric study are reported in this paper. The study focuses on four parameters of the acoustic scattering phenomenon. First, is the width of the axial splices. Our interest is to examine its effect on the energy flux of the scattered and transmitted wave modes. Our study suggests that if the width of the splices is not too narrow, the scattered modes essentially comprise of all the cut-on azimuthal modes and that the Sound Power Levels (PWLs) of the scattered modes are nearly the same. This finding is consistent with the equal energy assumption widely used in duct aeroacoustics. However, if the splice width is narrow, sound power level of the scattered duct modes is negligible. The second parameter investigated is the frequency of the incident duct mode. The results of our study show that the total sound power level of all the scattered modes would be significant relative to the transmitted incident mode if the frequency is slightly above the cut-on frequency. On the other hand, if the frequency is well above cut-on frequency, then the increase in the total sound power level of the scattered modes is relatively negligible.

The third parameter examined in this study is the number of splices. The results of our investigation reveal that a larger number of splices would result in a reduction in the sound power level of the scattered acoustic wave modes. This is important from the point of view of minimizing noise radiation. An explanation for the reduction is provided. The fourth parameter investigated is the length of the axial splices and the location at which most of the scattering takes place. Extensive computed results show that acoustic scattering by axial liner splices is a local phenomenon. Most of the scattering takes place primarily near the junction of the duct where the incident wave mode first encounters the spliced liner. Thus a long axial splice and a medium length splice have practically the same effect.

The rest of the paper is organized as follows. Section 2 presents the computational model and numerical methods used in this work. Since a time-domain approach is followed, the formulation of the time-domain impedance boundary condition and its implementation for spliced liner are described. To ensure the numerical simulation is accurate and of high quality, the numerical code is validated by comparing the computed results with those of Tester et al. [9]. Tester et al.'s results are calculated by the ACTRAN code. Section 3 reports the results of a parametric study. This study focuses on the effects of splice width, the frequency of the incident duct mode, the number and length of the splices on the scattering phenomenon. Section 4 summarizes the overall results of this work.

2. Computational model and numerical methods

In this section, we will introduce the physical and computational model used in this investigation. This is followed by a description of the computational methods. The present computer code is validated by comparing computed results with those of Tester et al. [9]. Tester et al. employed the ACTRAN code that is based on the finite element method.

2.1. Computational model

The computational model, consisting of a circular duct encased by spliced liner and hard walls, is shown in Fig. 1. A 3-D sketch of the spliced liner section is given in Fig. 2. The model was used previously by Regan and Eaton [3], McAlpine et al. [8] and Tester et al. [9]. The hard wall on the right represents the space between the fan blade and the spliced liner. The hard wall on the left represents the hard wall segment at the inlet of the

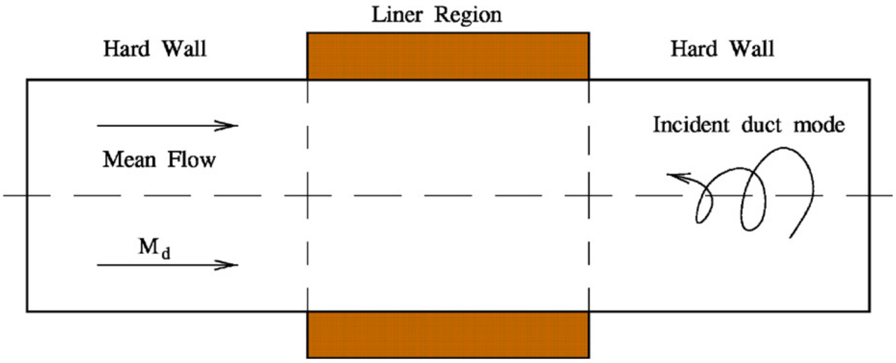

Fig. 1. Computation model.

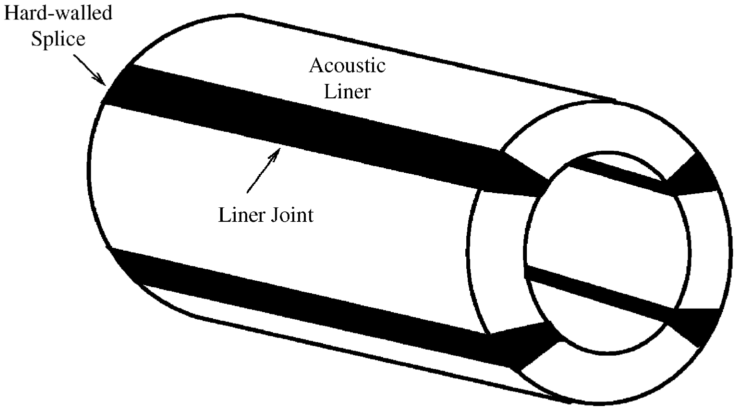

Fig. 2. Spliced liner model.

intake duct of a jet engine. The duct is assumed to have a constant diameter D (radius $a = D/2$). The duct carries a uniform mean flow at Mach number M_d. A spinning duct mode of azimuthal mode number m and frequency Ω (BPF or interaction tone frequency) propagates upstream from the fan face on the right of Fig. 1. The length of the liner is taken to be L. The resistance and reactance of the liner are R and X, respectively. It will be assumed that the number of hard wall splices is N_{seg}.

A spinning duct mode propagates upstream from the hard wall region of the duct on the right to the spliced liner segment. Acoustic scattering takes place as soon as the incident duct mode reaches the junction between the hard wall and the spliced liner. The N_{seg} rigid splices scatter the incident duct mode with azimuthal mode number m into spinning duct modes of the same frequency but with azimuthal mode number equal to $m \pm jN_{\text{seg}}$ ($j = 0,1,2,3,\ldots$). In addition to generating upstream propagating duct modes, there is back-scattering of rigid wall duct modes. Of interest is the intensity of the transmitted acoustic waves in the hard wall region upstream of the spliced liner.

2.2. Governing equations

Dimensionless variables are used in the computation. The scales used for non-dimensionalization purpose are:

D (diameter of the duct) = length scale,
a_0 (speed of sound of gas) = velocity scale,
D/a_0 = time scale,
ρ_0 (gas density) = density scale,
$\rho_0 a_0^2$ = pressure scale,
$\rho_0 a_0$ = impedance scale.

The duct is assumed to carry a uniform mean flow (in the positive x-direction) at a Mach number M_d. The acoustic disturbances inside the duct are governed by the linearized Euler equations. In cylindrical coordinates (r,ϕ,x) and velocity components (v,w,u), these equations are:

$$\frac{\partial \rho}{\partial t} + M_d \frac{\partial \rho}{\partial x} + \frac{\partial v}{\partial r} + \frac{v}{r} + \frac{1}{r}\frac{\partial w}{\partial \phi} + \frac{\partial u}{\partial x} = 0, \tag{1}$$

$$\frac{\partial v}{\partial t} + M_d \frac{\partial v}{\partial x} = -\frac{\partial p}{\partial r}, \tag{2}$$

$$\frac{\partial w}{\partial t} + M_d \frac{\partial w}{\partial x} = -\frac{1}{r}\frac{\partial p}{\partial \phi}, \tag{3}$$

$$\frac{\partial u}{\partial t} + M_d\frac{\partial u}{\partial x} = -\frac{\partial p}{\partial x}, \tag{4}$$

$$\frac{\partial p}{\partial t} + M_d\frac{\partial p}{\partial x} + \frac{\partial v}{\partial r} + \frac{v}{r} + \frac{1}{r}\frac{\partial w}{\partial \phi} + \frac{\partial u}{\partial x} = 0. \tag{5}$$

For a spinning duct mode with azimuthal mode number n, the solution may be written in the form:

$$\begin{bmatrix} \rho \\ u \\ v \\ w \\ p \end{bmatrix} = \mathrm{Re}\left\{ \begin{bmatrix} \hat{\rho}_n(r,x,t) \\ \hat{u}_n(r,x,t) \\ \hat{v}_n(r,x,t) \\ \hat{w}_n(r,x,t) \\ \hat{p}_n(r,x,t) \end{bmatrix} \mathrm{e}^{\mathrm{i}n\phi} \right\}, \tag{6}$$

where Re{ } is the real part of { }.

Substitution of Eq. (6) into Eqs. (1)–(5) gives the governing equations for $(\hat{\rho}_n, \hat{u}_n, \hat{v}_n, \hat{w}_n, \hat{p}_n)$

$$\frac{\partial \hat{\rho}_n}{\partial t} + M_d\frac{\partial \hat{\rho}_n}{\partial x} + \frac{\partial \hat{v}_n}{\partial r} + \frac{\hat{v}_n}{r} + \frac{\mathrm{i}n}{r}\hat{w}_n + \frac{\partial \hat{u}_n}{\partial x} = 0, \tag{7}$$

$$\frac{\partial \hat{v}_n}{\partial t} + M_d\frac{\partial \hat{v}_n}{\partial x} = -\frac{\partial \hat{p}_n}{\partial r}, \tag{8}$$

$$\frac{\partial \hat{w}_n}{\partial t} + M_d\frac{\partial \hat{w}_n}{\partial x} = -\frac{\mathrm{i}n}{r}\hat{p}_n \tag{9}$$

$$\frac{\partial \hat{u}_n}{\partial t} + M_d\frac{\partial \hat{u}_n}{\partial x} = -\frac{\partial \hat{p}_n}{\partial x} \tag{10}$$

$$\frac{\partial \hat{p}_n}{\partial t} + M_d\frac{\partial \hat{p}_n}{\partial x} + \frac{\partial \hat{v}_n}{\partial r} + \frac{\hat{v}_n}{r} + \frac{\mathrm{i}n}{r}\hat{w}_n + \frac{\partial \hat{u}_n}{\partial x} = 0. \tag{11}$$

2.3. Time-domain boundary conditions at the spliced liner surface

At the spliced liner surface, part of the surface is liner material and part of the surface is hard wall. On the part of the surface that is hard wall, the boundary condition is

$$r = a, \quad v = 0 \quad (a = D/2). \tag{12}$$

On the part of the surface with liner materials, time-domain impedance boundary condition is used. Let the surface impedance be ($\mathrm{e}^{-\mathrm{i}\omega t}$ time dependence assumed)

$$Z = R - \mathrm{i}X, \tag{13}$$

where R and X are the dimensionless resistance and reactance. Here the three parameters time-domain impedance boundary condition of Tam and Auriault [10] will be used. The reactance, which may be positive or negative, is parametrized by

$$X = \frac{X_{-1}}{\Omega} + X_1\Omega, \tag{14}$$

where Ω is the angular frequency of the incident sound. Numerical stability requires that $R>0$, $X_{-1}<0$ and $X_1>0$. Here for a given impedance value Z and frequency Ω, the two parameters of the model X_{-1} and X_1 are computed by the following formulas:

$$X_1 = \frac{1}{[(2/|Z|) - (X/|Z|^2)]\Omega}, \quad X_{-1} = \frac{-(1-(X/|Z|))^2\Omega}{[(2/|Z|) - (X/|Z|^2)]}. \tag{15}$$

It is easy to check that formula (15) satisfies Eq. (14) and the constraints on X_{-1} and X_1. Upon incorporating the Myers [11] convective term, the time-domain impedance boundary condition on the liner surface in a grazing flow at Mach M_d is

$$\frac{\partial p}{\partial t} + M_d \frac{\partial p}{\partial x} = R\frac{\partial v}{\partial t} - X_{-1}v + X_1 \frac{\partial^2 v}{\partial t^2}. \tag{16}$$

Now Eqs. (12) and (16) will be combined into a single spliced liner boundary condition. Let N_{seg} be the number of axial splices. Then the angle ϕ_{HW} subtended by a hard wall splice is equal to $2W/D$, where W is the width of a splice. Azimuthally, the spliced liner surface is a periodic function with period $2\pi/N_{\text{seg}}$.

Let $G(\phi)$ be a periodic function with period $2\pi/N_{\text{seg}}$ as shown in Fig. 3. $G(\phi)$ takes the value of 1 for $0<\phi<(2\pi/N_{\text{seg}}-\phi_{\text{HW}})$ and zero for $(2\pi/N_{\text{seg}}-\phi_{\text{HW}})<\phi<2\pi/N_{\text{seg}}$. The graph of $G(\phi)$ may be expanded in a Fourier series in ϕ,

$$G(\phi) = \sum_{s=-\infty}^{\infty} c_s \,\mathrm{e}^{\mathrm{i}sN_{\text{seg}}\phi}, \tag{17}$$

where

$$c_s = \begin{cases} \dfrac{\mathrm{i}}{2\pi s}\left(\mathrm{e}^{-\mathrm{i}s(2\pi-\phi_{\text{HW}}N_{\text{seg}})} - 1\right), & s\neq 0, \\ 1 - \dfrac{\phi_{\text{HW}}N_{\text{seg}}}{2\pi}, & s = 0. \end{cases} \tag{18}$$

Now the combined boundary condition of Eqs. (12) and (16) for the spliced liner may be written as

$$X_1\frac{\partial^2 v}{\partial t^2} + R\frac{\partial v}{\partial t} - X_{-1}v = G(\phi)\left[\frac{\partial p}{\partial t} + M_d\frac{\partial p}{\partial x}\right]. \tag{19}$$

It is easy to verify that on the liner surface, where $G(\phi) = 1.0$, Eq. (19) reduces to Eq. (16). On the surface of the rigid splices, where $G(\phi) = 0$, Eq. (19) reduces to

$$X_1\frac{\partial^2 v}{\partial t^2} + R\frac{\partial v}{\partial t} - X_{-1}v = 0. \tag{20}$$

It is straightforward to show, if the initial conditions

$$v = 0, \quad \frac{\partial v}{\partial t} = 0 \ \text{at} \ t = 0 \tag{21}$$

are imposed, the solution of Eq. (20) is $v = 0$, which is the rigid wall boundary condition.

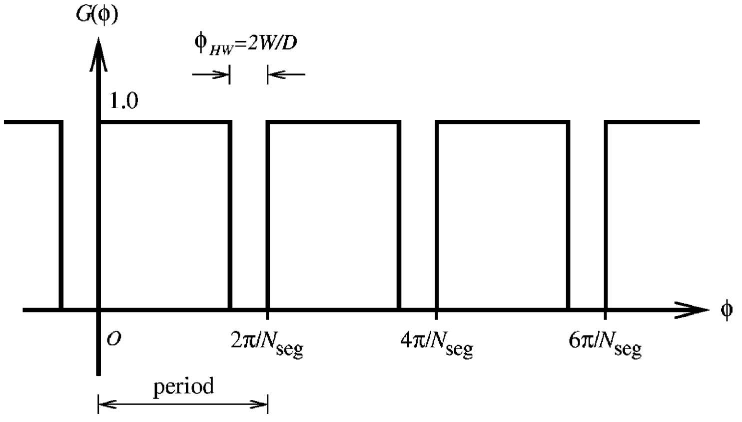

Fig. 3. Graph of function $G(\phi)$.

For convenience of enforcing boundary condition (19) at $r = D/2$, we will rewrite this equation as a system of first-order equation in t by introducing an auxiliary variable q defined by

$$\frac{\partial v}{\partial t} = q. \tag{22}$$

Eq. (19) may now be rewritten as

$$\frac{\partial q}{\partial t} = -\frac{R}{X_1}q + \frac{X_{-1}}{X_1}v - \frac{1}{X_1}G(\phi)\left[\frac{\partial v}{\partial r} + \frac{v}{r} + \frac{1}{r}\frac{\partial w}{\partial \phi} + \frac{\partial u}{\partial x}\right]. \tag{23}$$

In deriving Eq. (23), use has been made of Eq. (5). Finally, by replacing the time derivative of v in Eq. (2) at $r = D/2$ by q according to Eq. (22), the following time derivative free boundary condition is derived:

$$\frac{\partial p}{\partial r} = -q - M_d\frac{\partial v}{\partial x}. \tag{24}$$

In summary, the spliced liner surface boundary conditions at $r = D/2$ are Eqs. (22)–(24).

2.4. Computational algorithm

Due to scattering by the liner splices, the sound field inside the duct would consist of many azimuthal modes. The mode numbers are spaced by N_{seg} apart. The full solution inside the duct may be expressed in the form:

$$\begin{bmatrix} u(r,\phi,x,t) \\ v(r,\phi,x,t) \\ w(r,\phi,x,t) \\ p(r,\phi,x,t) \\ q(\phi,x,t) \end{bmatrix} = \text{Re}\left\{\sum_j \begin{bmatrix} \hat{u}_{m+j}(r,x,t) \\ \hat{v}_{m+j}(r,x,t) \\ \hat{w}_{m+j}(r,x,t) \\ \hat{p}_{m+j}(r,x,t) \\ \hat{q}_{m+j}(x,t) \end{bmatrix} e^{i(m+jN_{\text{seg}})\phi}\right\}, \tag{25}$$

where m is the azimuthal mode number of the incident duct mode.

The incident and scattered modes are coupled by the spliced liner surface boundary conditions (22)–(24). It is easy to see that only surface boundary condition (23) causes mode coupling. The amplitude functions of the incident and scattered duct modes of Eq. (25), i.e., $(\hat{u}_{m+j}, \hat{v}_{m+j}, \hat{w}_{m+j}, \hat{p}_{m+j})$ are calculated by Eqs. (8)–(11) with n replaced by $(m+jN_{\text{seg}})$. The values of $\hat{v}_{m+j}$ at $r = D/2$ are, however, not computed this way, since at this r location Eq. (8) has been effectively replaced by boundary condition (24). Each value of $\hat{v}_{m+j}$ is computed by a time marching method according to Eq. (22). Upon equating the azimuthal Fourier components in ϕ, Eq. (22) becomes

$$\frac{\partial \hat{v}_{m+j}}{\partial t} = \hat{q}_{m+j}. \tag{26}$$

To enforce boundary condition (24), the ghost-point method [12] is employed. For this purpose, a row of ghost value of p at $k = M+1$ is introduced. k is the mesh index in the r-direction. $k = M$ corresponds to $r = D/2$ as shown in Fig. 4. In the boundary region, at or adjacent to $k = M$, 7-point backward difference stencils are used to compute the r-derivative. The r-derivative stencils for all the variables, with the exception for p, terminate at $k = M$ (see Fig. 4). Those for p terminate at the ghost point $k = M+1$. The discretized form of Eq. (24) for each azimuthal mode, is (ℓ is the mesh index in the x-direction; superscript n is the time level),

$$\frac{1}{\Delta r}\sum_{s=-5}^{1} a_s^{15}\left(\hat{p}_{m+j}\right)_{\ell,M+s}^{(n)} = -\left(\hat{q}_{m+j}\right)_{\ell,M}^{(n)} - \frac{M_d}{\Delta x}\sum_{s=-3}^{3} a_s\left(\hat{v}_{m+j}\right)_{\ell+s,M}^{(n)}.$$

Thus on solving for the ghost value, $(\hat{p}_{m+j})_{\ell,M+1}^{(n)}$, it is found

$$\left(\hat{p}_{m+j}\right)_{\ell,M+1}^{(n)} = \frac{\Delta r}{a_1^{15}}\left[-\left(\hat{q}_{m+j}\right)_{\ell,M}^{(n)} - \frac{M_d}{\Delta x}\sum_{s=-3}^{3} a_s\left(\hat{v}_{m+j}\right)_{\ell+s,M}^{(n)} - \frac{1}{\Delta r}\sum_{s=-5}^{0} a_s^{15}\left(\hat{p}_{m+j}\right)_{\ell,M+s}^{(n)}\right] \tag{27}$$

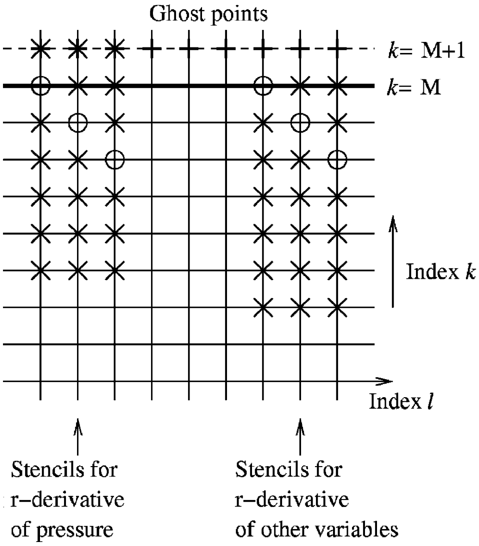

Fig. 4. Backward difference stencils and ghost points in the upper boundary region of the computational domain.

(for stencil coefficients a_s and backward difference stencil coefficients a_s^{15} see Ref. [12]). Eq. (27) is the formula by which the ghost values are found.

To implement the remaining boundary condition (23), the first step is to substitute Eq. (25) into Eq. (23) and equate terms according to the azimuthal mode number. This leads to an infinite system of equations. A finite system may be derived by dropping the azimuthal modes outside the range of importance. Suppose the scattered modes are limited to $-J\leqslant j\leqslant K$, then Eq. (23) leads to

$$\begin{aligned}\frac{\partial \hat{q}_{m+j}}{\partial t} = &-\frac{R}{X_1}\hat{q}_{m+j} + \frac{X_{-1}}{X_1}\hat{v}_{m+j}\\ &-\frac{1}{X_1}\sum_{\substack{-J\leqslant(j-s)\leqslant K\\ \text{sum over } s}} c_s\left[\frac{\partial \hat{v}_{m+j-s}}{\partial r} + \frac{\hat{v}_{m+j-s}}{r} + \frac{\mathrm{i}[m+(j-s)N_{\mathrm{seg}}]}{r}\hat{w}_{m+j-s} + \frac{\partial \hat{u}_{m+j-s}}{\partial x}\right]. \qquad (28)\end{aligned}$$

This is the equation for $\hat{q}_{m+j}$.

In this work, governing Eqs. (8)–(11) for each retained azimuthal mode ($m-J\leqslant n\leqslant m+K$) as well as Eqs. (26) and (28) are solved computationally by discretizing the system of equations according to the 7-point stencil DRP scheme [13]. To suppress possible numerical instability and to remove spurious short waves, artificial selective damping [14] is added to the discretized equations. It is known that time-domain impedance boundary condition with Myers [11] convective term included is subjected to Kelvin–Helmholtz instability [10]. This instability is suppressed by artificial selective damping. The computation is carried out on a Cartesian mesh in the $x-r$ plane within the computation domain as shown in Fig. 5. For each azimuthal mode, the axis boundary treatment developed by Shen and Tam [15] is imposed. This boundary treatment eliminates the apparent singularity of the system of Eqs. (8)–(11) at the axis ($r = 0$). At the duct wall ($r = D/2$) outside the spliced liner region, boundary condition (12) is used. This boundary condition is again enforced by the ghost-point method.

At the two open ends of the computation domain (see Fig. 5), perfectly matched layers (PML), as proposed by Hu [16] are added. The PML absorb all outgoing waves. On the right boundary, split variables are used to allow the incident duct mode to enter the computation domain from the PML region.

To start the computation, all variables are set equal to zero inside the computation domain. The incident acoustic wave mode propagates into the computation domain from the right. This begins the transient period of the computation. The computation continues and the numerical solution is monitored at a number of well-chosen locations. A stopping criterion is set based on how close the solution is to its former value at the

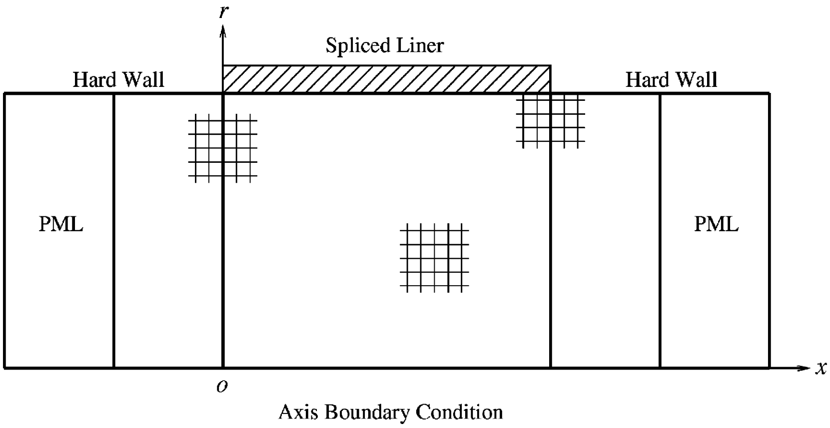

Fig. 5. The computational domain.

monitoring stations after a period according to the incident wave. Numerical results are measured only after further computation over a few more periods.

2.5. Code validation

For the purpose of validating the present time-domain code, the recently published results of Tester et al. [9] are used. Tester et al. computed their results by means of the ACTRAN code. ACTRAN is based on a finite element formulation. Details concerning mesh design and spatial resolution are provided in their work.

The resolution of the present time-domain code was tested by comparing the numerical results with exact solution for the case of a spinning acoustic mode propagating down a hard wall duct. Comparisons of the mode shape including more than one radial mode were made. Excellent agreements were found. The tests were conducted over a range of frequencies and azimuthal mode numbers. In addition to direct comparisons with exact analytical solution for hard wall duct modes, grid refinement tests were also carried out for ducts with spliced liners. The final mesh size adopted for the code yielded numerical solutions that were quite insensitive to mesh refinement.

Two cases are considered in the paper by Tester et al. [9]. One is at zero flow Mach number. The other case is at $M_d = 0.4$. The incident duct mode has a frequency equal to 1.1 cut-on frequency. Other details of their model problem are as follows:

Radius of duct (denoted by a) = $50''$ (127 cm).
Impedance of liner, $Z = 2 + \mathrm{i}$ (time factor = $\mathrm{e}^{-\mathrm{i}\Omega t}$).
Length of liner (L) = $24''$ or 60.96 cm ($L/a = 0.48$).
Number of splices = 2.
Width of splices = $3''$ (7.62 cm).
Azimuthal mode number of incident wave = 26.

2.5.1. No mean flow case

In this case, the frequency of the incident wave is 1331.9 Hz. Fig. 6 shows a comparison of the results of the present time-domain code and those of ACTRAN. This figure shows the axial distribution of PWL (same definition as in Morfey [17]) in dB (Re: PWL of incident wave mode at $x/a = 0.48$.) The spliced liner extends from $x/a = 0.0$ to 0.48. It is evident that the numerical results are in close agreement. This is true for the sound power level of the total transmitted sound as well as the incident and the individual scattered azimuthal modes. At the end of the spliced liner region ($x/a = 0.0$), the incident wave mode is significantly damped. Its sound power level is about 4 dB below that of the scattered wave modes.

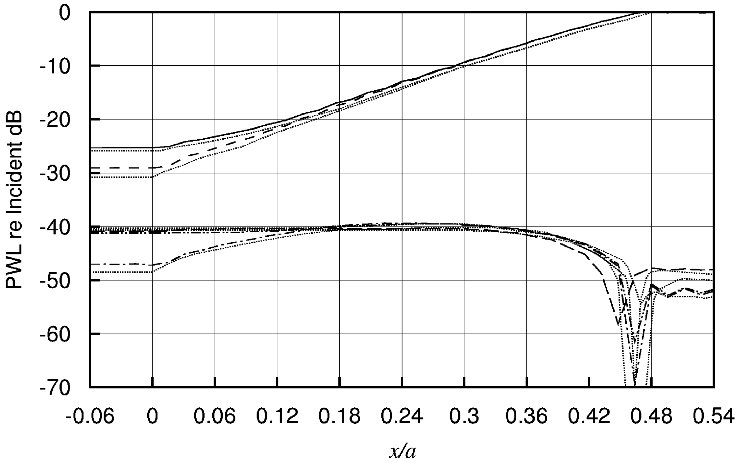

Fig. 6. Axial distribution of transmitted Sound Power Level (PWL). Flow Mach number = 0: (———) total PWL, present result; (– – – –) $m = 26$, (— · — · —) $m = 24$, (——–) $m = 22$, (— · · — · · —) $m = 20$; and (· · · · · · · ·) ACTRAN results.

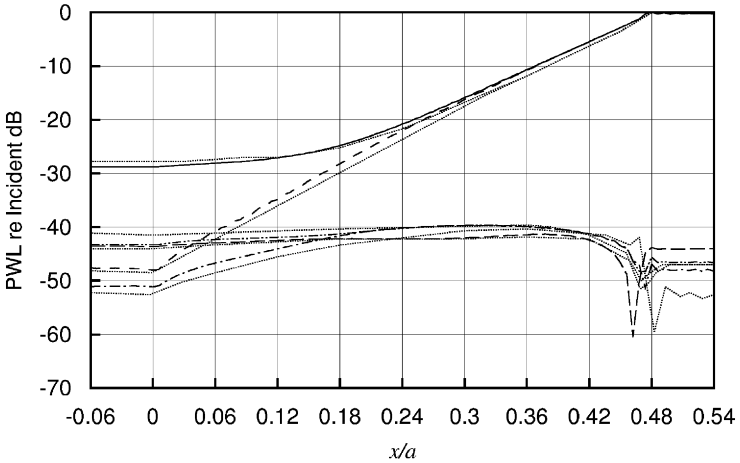

Fig. 7. Axial distribution of transmitted Sound Power Level (PWL). Flow Mach number = 0.4. (———) total PWL, present result; (– – – –) $m = 26$, (— · — · —) $m = 24$, (——–) $m = 22$, (— · · — · · —) $m = 20$; (· · · · · · · ·) ACTRAN results.

In the present computation, a grid refinement has been performed. The results reported here are regarded as grid converged.

2.5.2. Mach number 0.4 case

In this case, the frequency of the incident duct mode is 1220.7 Hz. Fig. 7 shows a comparison of the present computed axial distributions of sound power level and those of Tester et al. There are good agreements with respect to the total transmitted acoustic power as well as the sound power level of individual scattered azimuthal modes. This is true over the entire length of the acoustic liner. However, in the absence of error estimates from the ACTRAN code computation, it is not possible to ascertain the reason for the slight differences in the two sets of computed results.

3. A parametric study

A parametric study focused on four parameters of the spliced liner acoustic scattering phenomenon has been carried out. The study concentrates on the following effects and questions.

3.1. Effect of splice width

In this study, the effect of the width of the splices on the effectiveness of acoustic scattering is examined. Fig. 8 shows a comparison of the axial distribution of the total transmitted PWL for the test case specified in Section 2.5 (the same test conditions as Tester et al.) at a mean flow Mach number 0.4 and different splice widths. In addition to the case with splice width equal to 3″ or 7.62 cm (shown in Fig. 7), the cases of 1″ (2.54 cm), 0.5″ (1.27 cm) and 0″ (uniform liner) are also shown. Clearly, as anticipated, the intensity of scattered acoustic waves increases with splice width, all other variables are held fixed. For splice width 0.5″ (1.27 cm) and narrower, there is little acoustic scattering.

To obtain a better understanding of the scattering phenomenon, the distribution of total transmitted PWL for all azimuthal modes at the hard wall region upstream of the acoustic liner is plotted in Fig. 9 for the splices with 3″ (7.62 cm) width. It is easy to see that the scattered wave energy is concentrated in the propagating azimuthal modes (here a mode is loosely referred to as a propagating mode if it is a propagating mode in a solid wall duct of the same diameter). The sound power level of the propagating

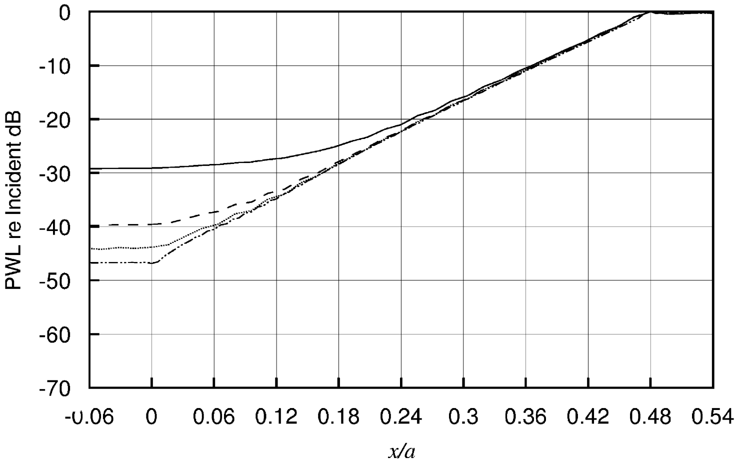

Fig. 8. Comparison of the transmitted Sound Power Level (PWL) for liner with two splices. Splice width: (———) 3″ (7.62 cm); (– – – –) 1″ (2.54 cm); (· · · · · · · ·) 0.5″ (1.27 cm); and (— · · — · · —) 0″.

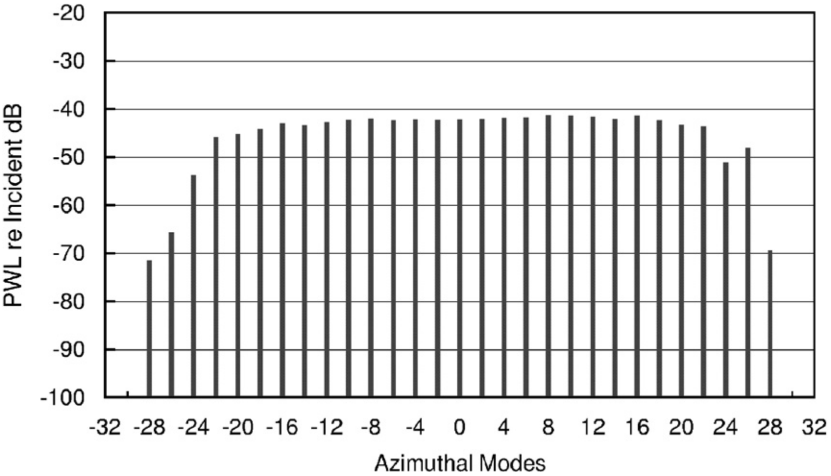

Fig. 9. Distribution of total transmitted Sound Power Level (PWL) in azimuthal modes in the region upstream of the spliced liner. Two 3″ (7.62 cm) splices.

modes of the scattered waves is almost the same. In this case, the level of each scattered mode is higher than that of the incident wave mode. Figs. 10 and 11 show similar results for splices with a width of 1″ (2.54 cm) and 1/2″ (1.27 cm), respectively. Again, most of the transmitted energy of the scattered modes is concentrated on the propagating modes. The level of the propagating modes is again nearly constant. In both of these cases, the incident wave mode has amplitude higher than that of the scattered modes.

Figs. 12–14 show the distribution of sound power level in radial modes for the $m = 0$, 8 and 16 azimuthal modes of Fig. 9. These figures reveal that most of the acoustic energy of an azimuthal mode is concentrated in the high-order propagating radial modes. This energy concentration in the high-order radial modes turns out to be true in all the cases computed in the present parametric study. Since the energy of low order modes is concentrated near the duct wall whereas that of the high-order modes is spread out more evenly over the cross section of the duct, the scattering phenomenon has the tendency to equalize energy distribution in a duct.

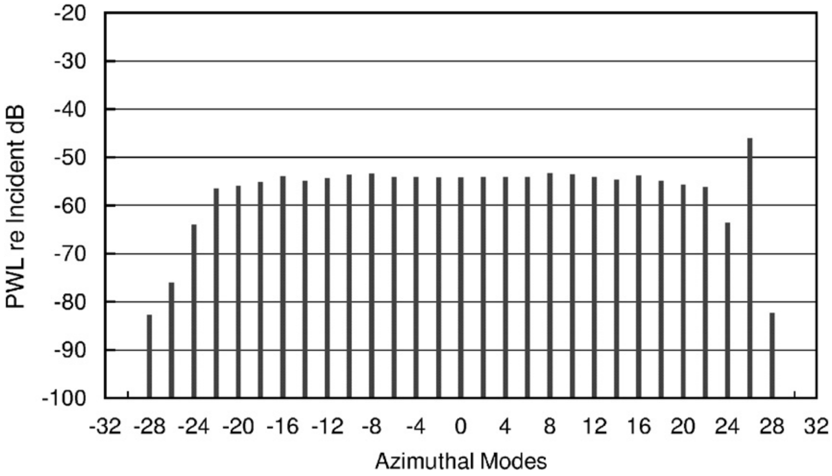

Fig. 10. Distribution of total transmitted Sound Power Level (PWL) in azimuthal modes in the region upstream of the spliced liner. Two 1″ (2.54 cm) splices.

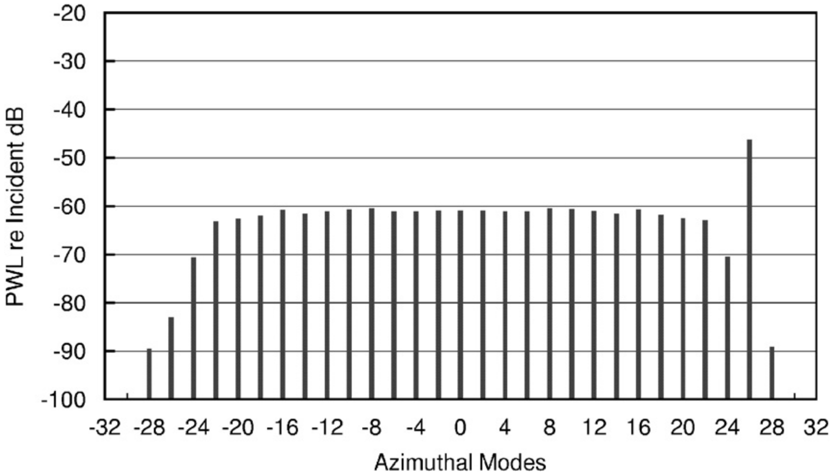

Fig. 11. Distribution of total transmitted Sound Power Level (PWL) in azimuthal modes in the region upstream of the spliced liner. Two 0.5″ (1.27 cm) splices.

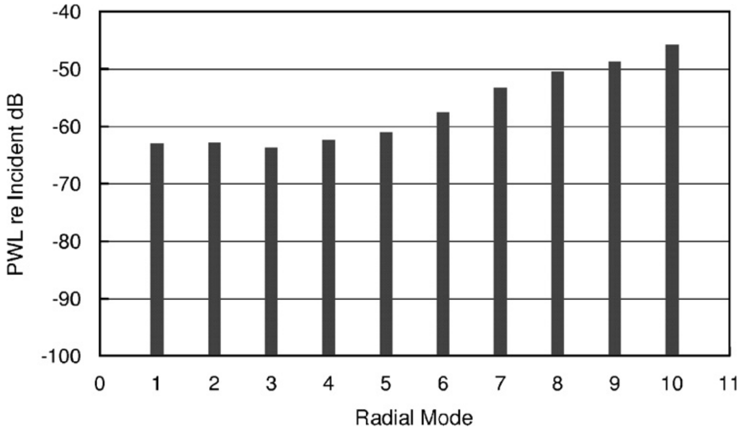

Fig. 12. Distribution of total transmitted Sound Power Level (PWL) in radial modes for azimuthal mode $m = 0$ in the region upstream of the spliced liner. Two 3″ (7.62 cm) splices.

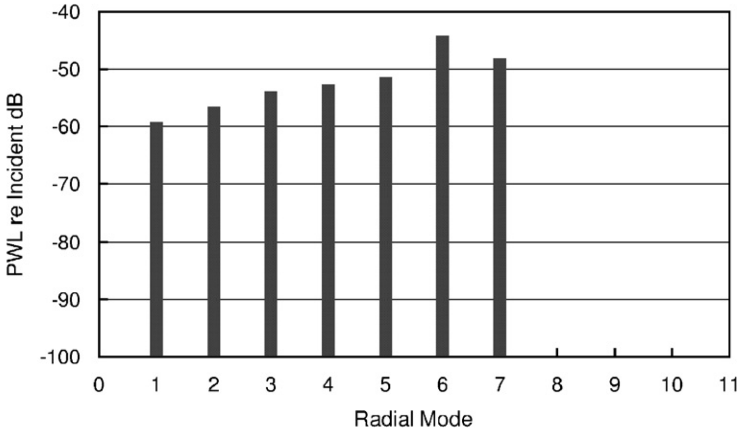

Fig. 13. Distribution of total transmitted Sound Power Level (PWL) in radial modes for azimuthal mode $m = 8$ in the region upstream of the spliced liner. Two 3″ (7.62 cm) splices.

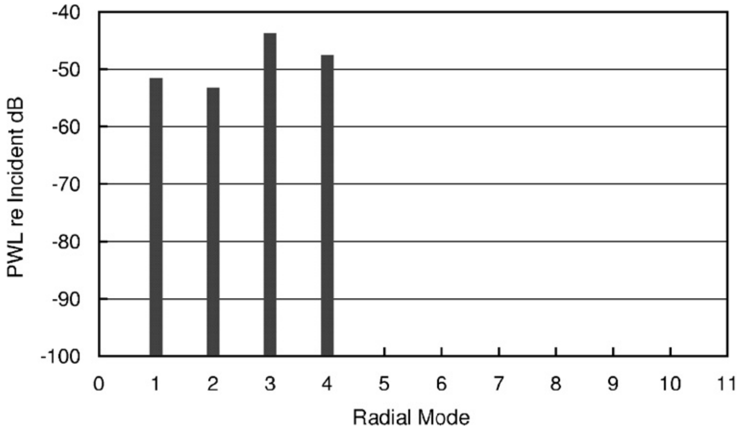

Fig. 14. Distribution of total transmitted Sound Power Level (PWL) in radial modes for azimuthal mode $m = 16$ in the region upstream of the spliced liner. Two 3″ (7.62 cm) splices.

3.2. Effect of frequency

How important is frequency as a parameter of the spliced liner scattering phenomenon? To examine the effect of frequency, 3 cases are studied using the Tester et al. problem but at 1.5, 1.1 and 0.9 cut-on frequency. Fig. 15 shows the axial distribution of the sound power level of the incident wave mode, the sum of the sound power level of all waves and those of a few selected scattered waves at a 1.5 cut-on frequency. It is clear from the results shown that at high frequency, because the spatial damping rate in the lined section is small, the amplitude of the total acoustic wave is nearly the same as that of the incident wave mode ($m = 26$). Thus acoustic scattering is not important. Fig. 16 shows the distribution of sound power level of all the transmitted waves in azimuthal modes. The sound power level of the scattered wave modes is over 30 dB below that of the incident mode.

The case of incident wave at a slightly above cut-on frequency is shown in Fig. 17. It is to be noted that at this frequency the total sound power level of the transmitted scattered waves is 19 dB higher than that of the incident mode. Fig. 18 shows similar axial distribution at 0.9 cut-on frequency. In this case the incident wave

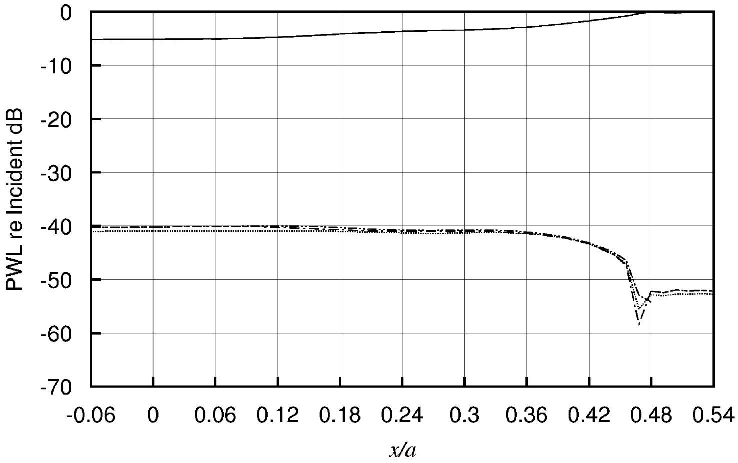

Fig. 15. Axial distribution of Sound Power Level (PWL). Flow Mach number = 0.4. Two 3″ (7.62 cm) splices. Frequency = 1664 Hz; frequency = 1.5 cut-on frequency. (———) total PWL; (– – – –) $m = 26$; (· · · · · · · ·) $m = 24$; (— · — · —) $m = 22$; (— · · — · · —) $m = 20$.

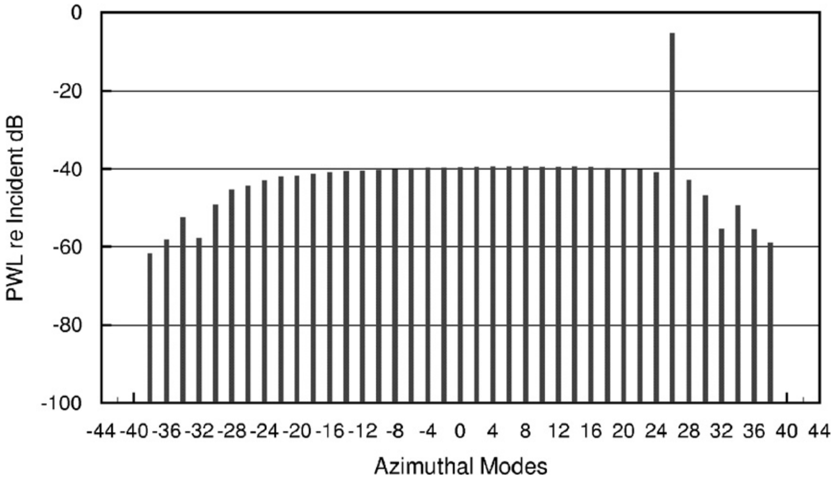

Fig. 16. Distribution of sound power level in azimuthal modes upstream of the spliced liner. Frequency = 1664 Hz; frequency = 1.5 cut-on frequency.

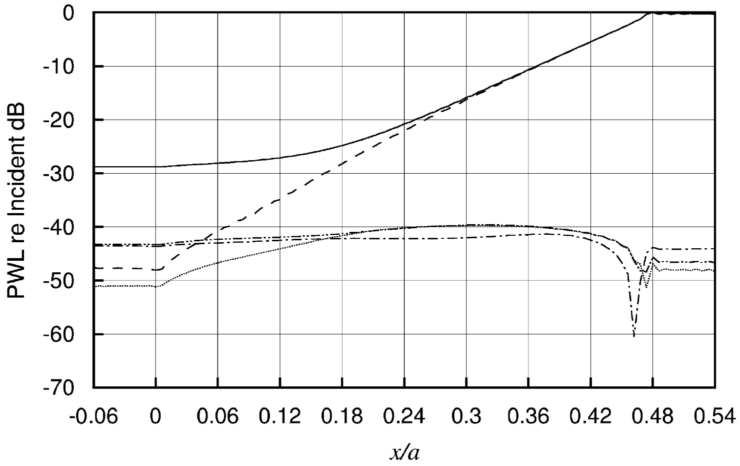

Fig. 17. Axial distribution of sound power level. Flow Mach number = 0.4. Two 3″ (7.62 cm) splices. Frequency = 1221 Hz; frequency = 1.1 cut-on frequency: (———) total Sound Power Level (PWL); (– – –) $m = 26$; (· · · · · · · ·) $m = 24$; (— · — · —) $m = 22$; and (— · · — · · —) $m = 20$.

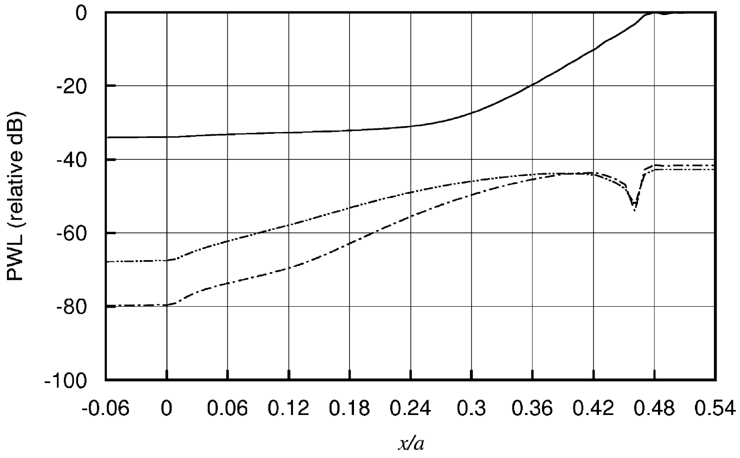

Fig. 18. Axial distribution of sound power level. Flow Mach number = 0.4. Two 3″ (7.62 cm) splices. Frequency = 998.8 Hz; frequency = 0.9 cut-on frequency: (———) total Sound Power Level (PWL); (— · — · —) $m = 22$; and (— · · — · · —) $m = 20$.

mode is heavily damped. At the end of the liner region, only the scattered waves remain. Fig. 19 shows the distribution of sound power level of the total transmitted waves in azimuthal modes. The intensity of the scattered waves is comparable to the case at 1.1 cut-on frequency. Acoustic scattering is, without question, important for incident mode at below cut-on frequency. It is to be noted that sound power level for a cut-off mode in the hard wall region is zero. However, the sound power level of the combined incident and reflected cut-off modes is not zero. Here this is used as the reference level for computing relative sound power level in Figs. 18 and 19.

3.3. Effect of number of splices

Suppose the total width of hard wall splices is fixed. Is it advantageous to use a larger number of narrower splices? For instance, in the problem considered by Tester et al. the total splice width is 6″ (15.24 cm). By

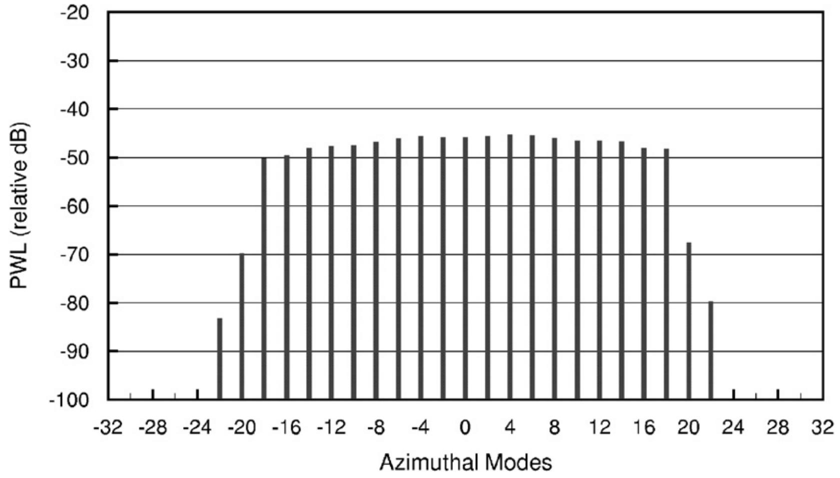

Fig. 19. Distribution of total transmitted Sound Power Level (PWL) in azimuthal modes upstream of the spliced liner. Frequency = 998.8 Hz; frequency = 0.9 cut-on frequency.

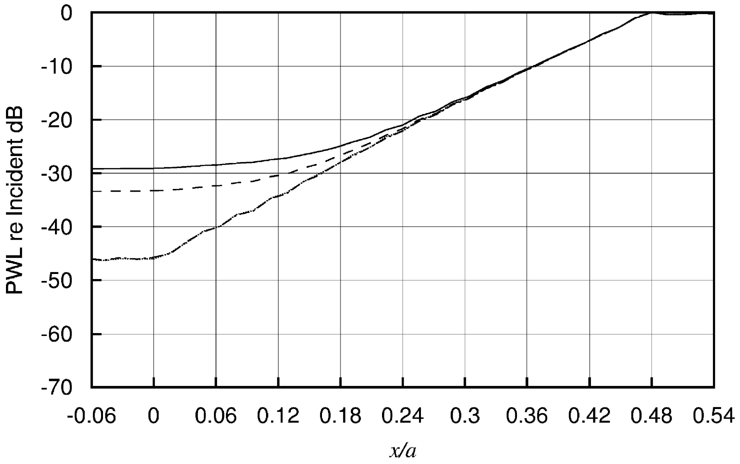

Fig. 20. Axial distribution of sound power level. Flow Mach number = 0.4. Total width of splices = 6″ (15.24 cm). Frequency = 1221 Hz; frequency = 1.1 cut-on frequency. (———) two splices, total Sound Power Level (PWL); (· · · · · · ·) two splices, $m = 26$; (– – – –) four splices, total PWL; (— · — · —) four splices, $m = 26$.

keeping the total width at 6″ (15.24 cm), one can use two 3″ (7.62 cm) splices or four 1.5″ (3.81 cm) splices. Fig. 20 shows the axial distributions of the sound power level of the total transmitted waves for both cases. It is evident that there is more than 3 dB less transmitted sound when four splices are used. In other words, there is a definite advantage in using a larger number of splices for a fixed total width. As another example, Fig. 21 shows the results of the same problem but for a total splice width of 12″ (30.48 cm). In this figure, the axial distributions of the sound power level of the transmitted waves for two 6″ (15.24 cm) splices and four 3″ (7.62 cm) splices are provided. It is clear that the use of more splices has an advantage of slightly over 3 dB.

The reason why there is an advantage in using a larger number of splices can be found by examining the distribution of sound power level of the total transmitted waves in azimuthal modes. Figs. 22 and 23 show the distribution for the case of two 3″ (7.62 cm) spliced and four 1.5″ (3.81 cm) splices. For both cases, the transmitted acoustic energy is associated mainly with the propagating modes as mentioned before. It is to be noted that the levels of the propagating azimuthal modes are about the same for both cases. Now for the four splices configuration, the scattered azimuthal modes have mode numbers separated by 4 (i.e. $m = 26 \pm 4j$,

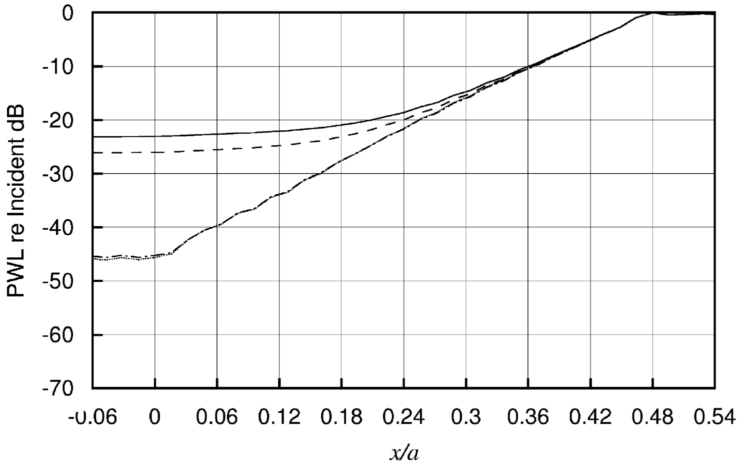

Fig. 21. Axial distribution of sound power level. Flow Mach number = 0.4. Total width of splices = 12″ (30.48 cm). Frequency = 1221 Hz; frequency = 1.1 cut-on frequency: (———) two splices, total Sound Power Level (PWL); (· · · · · · · ·) two splices, $m = 26$; (– – – –) four splices, total PWL; (— · — · —) four splices, $m = 26$.

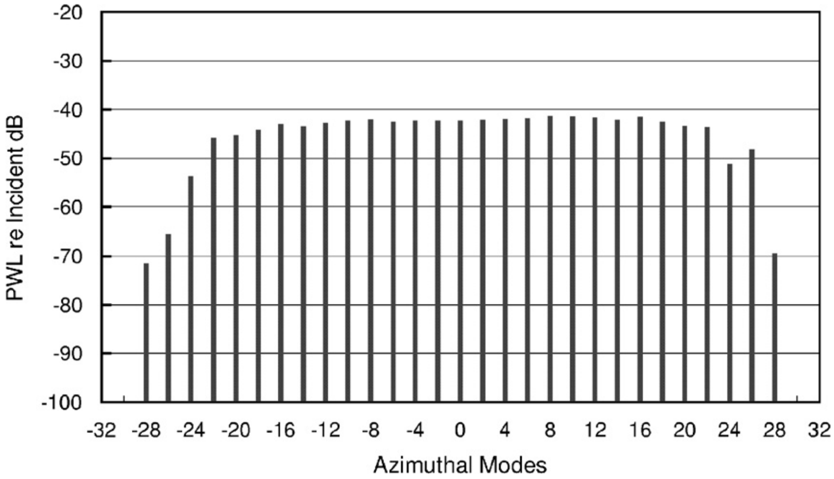

Fig. 22. Distribution of sound power level in azimuthal modes upstream of the spliced liner. Two 3″ (7.62 cm) splices. Frequency = 1221 Hz.

$j = 0,1,2,\ldots$) while those for the 2 splices configuration have mode numbers separated by 2 (i.e. $m = 26 \pm 2j$, $j = 0,1,2,\ldots$). Thus there are nearly twice as many propagation azimuthal modes for the two splices configuration as the four splices configuration. This difference accounts for 3 dB less transmitted wave energy for the four splices configuration. Figs. 24 and 25 show similar distribution of sound power level in azimuthal modes for the two 6″ (15.24 cm) splices and the four 3″ (7.62 cm) splices configurations. Again, the two splice configuration has nearly twice as many propagating azimuthal modes. This results in 3 dB more in the total transmitted acoustic energy.

3.4. Effect of splice length

Extensive computation of the spliced liner acoustic scattering phenomenon suggests that scattering is confined mainly to the region close to the junction between the hard wall and the spliced liner near the fan face. To demonstrate that scattering is, indeed, a local phenomenon, the scattering problem of Tester et al. is reconsidered with the modification that the splices have a length shorter than the acoustic liner. Fig. 26 shows

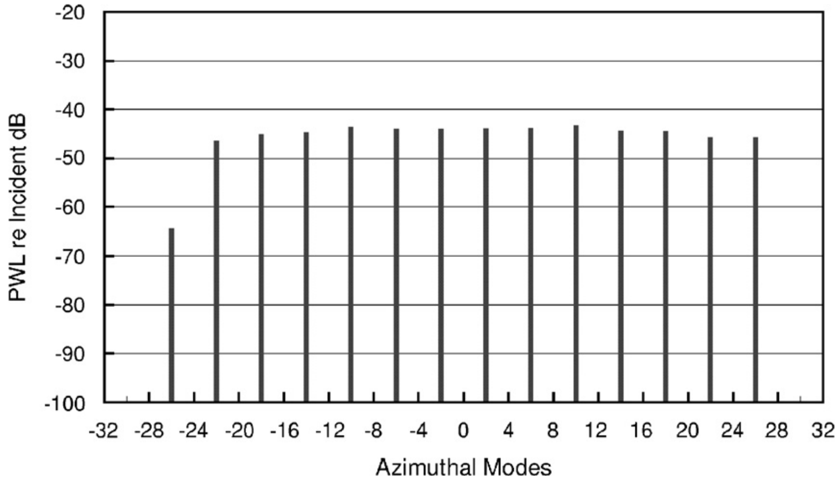

Fig. 23. Distribution of sound power level in azimuthal modes upstream of the spliced liner. Four 1.5″ (3.81 cm) splices. Frequency = 1221 Hz.

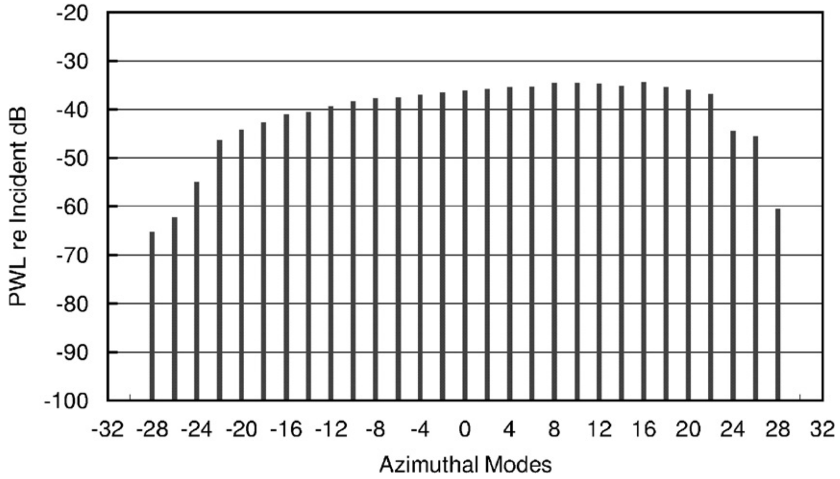

Fig. 24. Distribution of sound power level in azimuthal modes upstream of the spliced liner. Two 6″ (15.24 cm) splices. Frequency = 1221 Hz.

a 3-D view of the modified configuration of the spliced liner. Fig. 27 shows the computation domain of the modified configuration. Fig. 28 shows the axial distributions of sound pressure level of the total transmitted acoustic waves for the four cases with hard wall splice length equal to 24″ (60.96 cm, same length as the liner), 12″ (30.48 cm), 6″ (15.24 cm) and 0″ (no splice). It is readily seen that the transmitted acoustic energy is nearly identical for splice length of 12″ (30.48 cm) and 24″ (60.96 cm). The axial distribution differs only slightly for splice length of 6″ (15.24 cm). This result strongly indicates that most of the acoustic scattering takes place over a length of approximately 6″ (15.24 cm) to 8″ (20.32 cm).

Fig. 29 shows the distribution of the sound pressure level of the transmitted sound in azimuthal modes at the upstream hard wall region of the duct for splice length equal to 6″ (15.24 cm), 12″ (30.48 cm) and 24″ (60.96 cm). Again, it is readily seen the intensities of the scattered propagating wave modes are nearly the same regardless whether the splice length is 12″ (30.48 cm) or 24″ (60.96 cm). The intensities are slightly reduced for

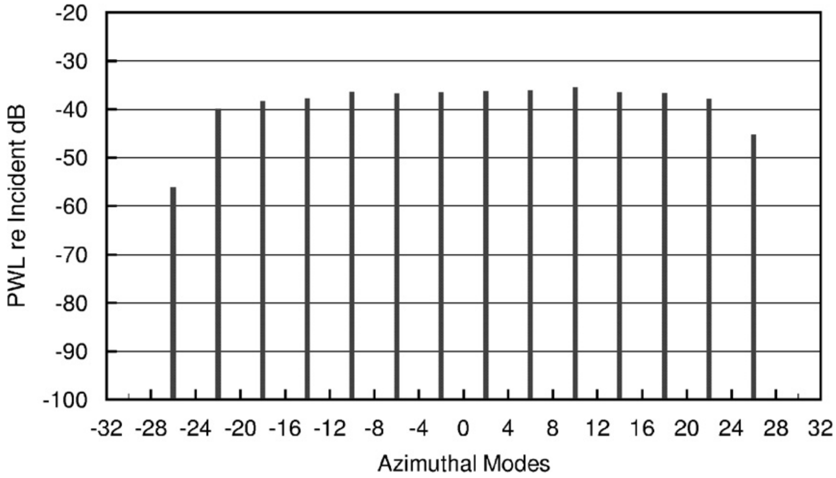

Fig. 25. Distribution of sound power level in azimuthal modes upstream of the spliced liner. Four 3″ (7.62 cm) splices. Frequency = 1221 Hz.

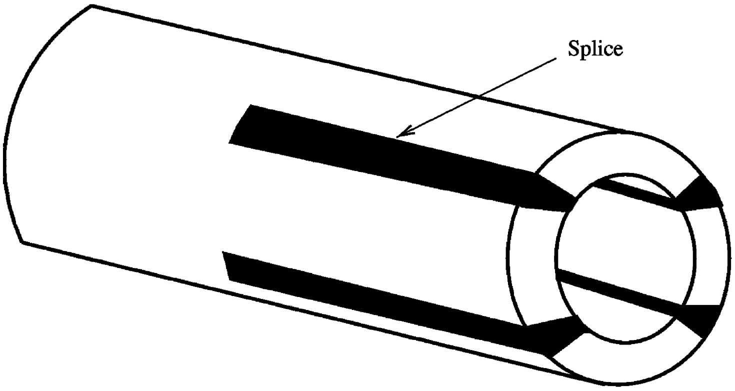

Fig. 26. Modified spliced liner model.

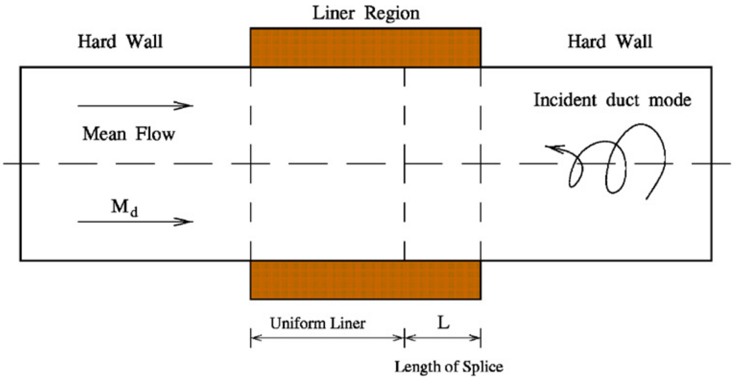

Fig. 27. Modified computational model.

the 6″ (15.24 cm) length splices. The fact that there is almost no difference between the 12″ (30.48 cm) and 24″ (60.96 cm) long splices further confirms the belief that acoustic scattering is quite local. There is little scattering beyond the first 12″ (30.48 cm) measured from the downstream end of the acoustic liner.

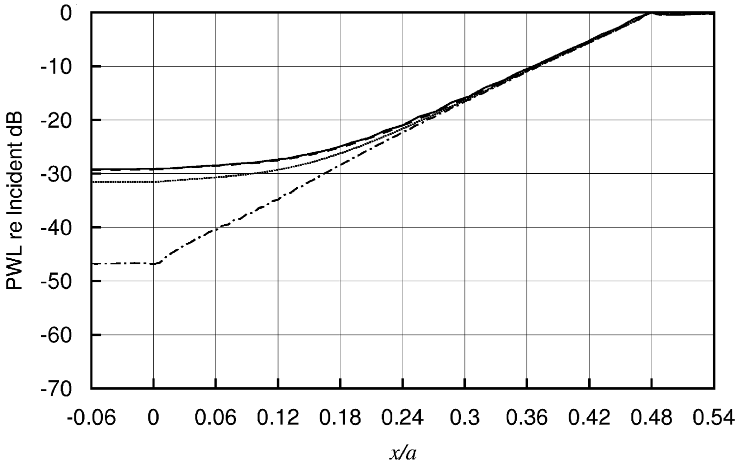

Fig. 28. Axial distribution of sound power level. Flow Mach number = 0.4. Two 3″ (7.62 cm) wide splices. Frequency = 1221 Hz. Splice length: (———) 24″ (60.96 cm); (– – – –) 12″ (30.48 cm); (· · · · · · · ·) 6″ (15.24 cm); (— · — · —) 0″.

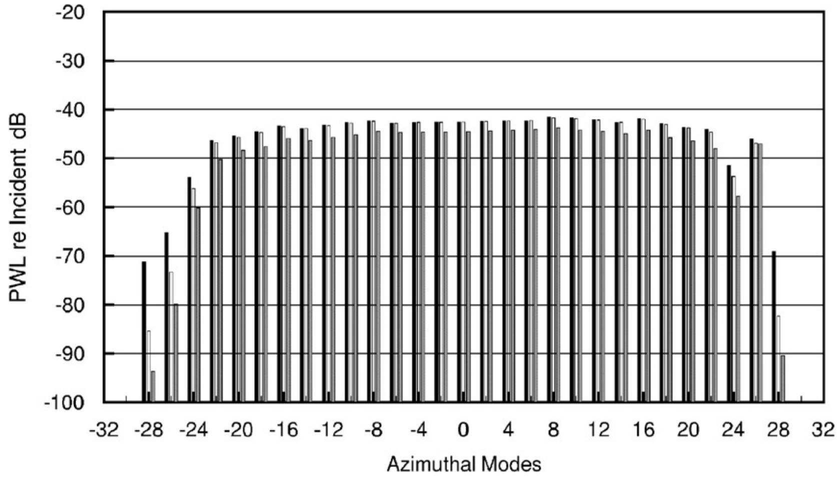

Fig. 29. Distribution of sound power level in azimuthal modes upstream of the spliced liner. Two 3″ (7.62 cm) wide splices. Frequency = 1221 Hz. Black filled bar: splice length 24″ (60.96 cm); hollow bar: splice length 12″ (30.48 cm); gray filled bar: 6″ (15.24 cm).

4. Summary

The scattering of acoustic duct modes by axial liner splices is a rather complex phenomenon. It is influenced by a host of parameters. This work concentrates on the study of four aspects of the phenomenon. The effect of splice width is first examined. It is found that scattering increases with splice width. However, for a typical modern day jet engine, scattering is not important if the splice width is less than 0.5″ (1.77 cm). Extensive computations indicate that scattering by liner splices tends to result in relatively uniform distribution of scattered wave energy inside the duct. It is observed that all the scattered cut-on azimuthal modes, generally, have nearly equal amplitude. In addition, for each cut-on azimuthal mode, the high-order cut-on radial mode consistently has the high amplitude in all the computed results. These high-order radial modes have a more even energy distribution across the cross-section of the duct whereas low order radial modes concentrate their energy and fluctuations close to the duct wall.

Whether the scattering phenomenon under study significantly increases the transmitted wave energy depends strongly on the incident mode frequency. For duct modes at a frequency much higher than the cut-on frequency, the amplitude of the incident mode is, generally, not damped by the liner. Because of this, the total energy of the scattered modes is small compared to that of the incident mode at the inlet of the duct. Thus scattering by liner splices have little effect on the radiated noise. At slightly above cut-on frequency, an incident duct mode would be heavily damped unless the liner is very short. On the other hand, the cut-on scattered modes would not experience significant damping by the liner. In this case, the scattered wave modes could cause a large increase in the transmitted acoustic wave energy when compared with that of the liner without splices. This is extremely undesirable. At below cut-on frequency, the energy of the scattered cut-on modes at the duct inlet is usually larger than that of the incident mode. To minimize the effect of scattering, it is recommended that liner splices be installed far away from the fan face.

If the surface area of liner splices is kept fixed, then it is advantageous to use a large number of narrow splices. This is because the azimuthal mode number of the scattered mode are spaced further apart when there is a larger number of splices. In other words, when there are more splices, although they are narrower, there are fewer scattered cut-on azimuthal modes. Since the magnitudes of the energy of the scattered cut-on azimuthal modes tend to be more or less the same, the result is that the transmitted wave energy is less when there are more splices.

The present study establishes that acoustic scattering by liner splices is a local phenomenon. For modern commercial jet engines, most scattering takes place over a short length of the splices (approximately 12″ or 30.48 cm in length). The remaining length of the splices does not seem to cause further increase in the energy of the scattered waves.

Finally, a search of the literature reveals that most previous works on scattering by liner splices use the frequency-domain approach in their computation. The present investigation is one of the first to perform all computations in the time domain. It is demonstrated that time-domain results are as accurate as those of high quality frequency-domain computation. Time-domain computation has the intrinsic advantages that nonlinear effects as well as broadband sound may easily be included in the calculation. However, due to the limited scope of this work, these advantages have yet to be demonstrated.

Acknowledgment

The authors wish to thank the Florida State University for permission to use their SP-4 supercomputer.

References

[1] C.R. Fuller, Propagation and radiation of sound from flanged circular ducts with circumferentially varying wall admittances, I: semi-infinite ducts, *Journal of Sound and Vibration* 93 (1984) 321–340.

[2] C.R. Fuller, Propagation and radiation of sound from flanged circular ducts with circumferentially varying wall admittances, II: finite duct with sources, *Journal of Sound and Vibration* 93 (1984) 341–351.

[3] B. Regan, J. Eaton, Modelling the influence of acoustic liner non-uniformities on duct modes, *Journal of Sound and Vibration* 219 (1999) 859–879.

[4] T. Elnady, H. Boden, R. Glav, Application of the point matching method to model circumferentially segmented non-locally reacting liners, AIAA Paper 2001-2202, 2001.

[5] T. Elnady, H. Boden, Hard strips in lined ducts, AIAA Paper 2002-2444, 2002.

[6] W.P. Bi, V. Pagneux, D. Lafarge, Sound propagation in varying cross-section ducts lined with non-uniform impedance by multimode propagation method, AIAA Paper 2005-3066, 2005.

[7] W.P. Bi, V. Pagneux, D. Lafarge, Y. Auregan, Characteristics of penalty mode scattering by rigid splices in lined ducts, AIAA Paper 2005-2897, 2005.

[8] A. McAlpine, M.C.M. Wright, H. Batard, S. Thezelais, Finite/boundary element assessment of a turbofan spliced intake liner at supersonic fan operating conditions, AIAA Paper 2003-3305, 2003.

[9] B.J. Tester, C.J. Powles, N.J. Baker, A.J. Kempton, Scattering of sound by liner splices: a Kirchhoff model with numerical verification, *AIAA Journal* 44 (2006) 2009–2017.

[10] C.K.W. Tam, L. Auriault, Time-domain impedance boundary conditions for computational aeroacoustics, *AIAA Journal* 34 (1996) 917–923.

[11] M. Myers, On the acoustic boundary condition in the presence of flow, *Journal of Sound and Vibration* 71 (1980) 429–434.

[12] C.K.W. Tam, Z. Dong, Wall boundary conditions for high order finite difference schemes in computational aeroacoustics, *Journal of Theoretical and Computational Fluid Dynamics* 6 (1994) 303–322.

[13] C.K.W. Tam, J.C. Webb, Dispersion-relation-preserving finite difference scheme for computational acoustics, *Journal of Computational Physics* 107 (1993) 262–281.

[14] C.K.W. Tam, J.C. Webb, Z. Dong, A study of the short wave components in computational acoustics, *Journal of Computational Acoustics* 1 (1993) 1–30.

[15] H. Shen, C.K.W. Tam, Three-dimensional simulation of the screech phenomenon, *AIAA Journal* 40 (2002) 33–41.

[16] F.Q. Hu, A stable perfectly matched layer for linearized Euler equations in unsplit physical variables, *Journal of Computational Physics* 173 (2001) 455–480.

[17] C.L. Morfey, Acoustic energy in non-uniform flows, *Journal of Sound and Vibration* 14 (1971) 159–170.